applied sciences

MDPI

Article

Analysis of the Near-Ground Wind Field Characteristics during Typhoon Soulik

Xu Wang [1,2], Zhilan Yao [1,2], Yun Guo [3,*] and Yongguang Li [1,2]

[1] State Key Laboratory of Mountain Bridge and Tunnel Engineering, Chongqing Jiaotong University, Chongqing 400074, China; xuwang@cqjtu.edu.cn (X.W.); zhilanyao0522@163.com (Z.Y.); yongguangli@mails.cqjtu.edu.cn (Y.L.)
[2] School of Civil Engineering, Chongqing Jiaotong University, Chongqing 400041, China
[3] School of Civil Engineering, Central South University, Changsha 410075, China
* Correspondence: guoy951214@163.com

Abstract: In 2013, during Typhoon Soulik, wind data were collected at various heights above the ground (15, 27, 53, 67, and 82 m) on the 550 kV 52# pole transmission tower in Ningde City, Fujian Province. The wind speed profile, turbulence intensity, gust factor, crest factor, and power spectrum were analyzed using 10 min interval wind speed records. The results show the following: (1) the average wind velocity of Typhoon Soulik varies in accordance with both the power law and the logarithmic law, but the Deaves–Harris model exhibits significant discrepancies; (2) the turbulence intensity in u, v, and w orientations decreases with the average wind velocity at each height. Exponential fitting is conducted on the strength of turbulence and gust factor profiles in each direction based on the standards of different countries, resulting in the derivation of empirical expressions; (3) the integral scale components of turbulence in u, v, and w orientations exhibit a positive correlation with both average wind velocity and height. The turbulence integral scale ratios in the longitudinal, transverse, and vertical directions at heights of 15, 53, and 82 m are 1:0.68:0.11, 1:0.67:0.27, and 1:0.67:0.30, respectively; (4) the Von Karman empirical spectrum and the modified Kaimal cross-spectrum model closely match the observed wind power spectrum of Typhoon Soulik. The presented results contribute to furthering references for wind-resistant design of structures in typhoon-prone areas and prevention of typhoon-related disasters.

Keywords: typhoon Soulik; wind speed profile; turbulence strength; gust factor; power spectrum

check for updates

Citation: Wang, X.; Yao, Z.; Guo, Y.; Li, Y. Analysis of the Near-Ground Wind Field Characteristics during Typhoon Soulik. *Appl. Sci.* **2024**, *14*, 4001. https://doi.org/10.3390/app14104001

Academic Editor: Tianyou Tao

Received: 22 April 2024
Revised: 6 May 2024
Accepted: 7 May 2024
Published: 8 May 2024

Copyright: © 2024 by the authors. Licensee MDPI, Basel, Switzerland. This article is an open access article distributed under the terms and conditions of the Creative Commons Attribution (CC BY) license (https://creativecommons.org/licenses/by/4.0/).

1. Introduction

Typhoons are highly devastating natural calamities that result in significant economic damages and casualties in coastal regions worldwide on an annual basis [1,2]. The rapid growth of urban construction has led to the emergence of several high-rise buildings and other wind-sensitive structures. The wind characteristics near the ground have become a critical factor in the engineering design process [3,4]. Therefore, it is imperative to examine the characteristics of the wind field near the ground during powerful typhoons to establish a scientific foundation for designing buildings that can withstand heavy winds [5].

The study of wind characteristics commonly utilizes wind tunnel experiments, numerical modeling, and field measurement [6,7]. However, simulating typhoons in experiments is difficult. Field measurement is considered the most reliable method for investigating typhoons. In addition to providing wind field data, they avoid the modelling and scaling errors implicit in numerical simulations and wind tunnel tests [8].

Over the past few years, numerous researchers both domestically and internationally have conducted extensive studies through field measurements. The dominant method in wind engineering for field measurement of typhoons is to place ultrasonic anemometers on anemometer towers [9,10]. For example, Song et al. [11] employed six wind towers within heights of 110 m to carry out field measurements of the powerful typhoons Hagupit, Nesat, and Rammasun. The result shows that the profile of the typhoons' winds departed from the power law to different extents. Lin et al. [12] fitted the turbulence intensity profiles in front and behind the typhoon based on the measurement results of three anemometers at 10, 26, and 32 m above the anemometer tower and found that the fitting results had the smallest difference with Chinese standards. Fang et al. [13] analyzed the data collected from four meteorological towers using mechanical anemometers to examine the gust characteristics of 10 typhoon winds near the ground. They discovered that the fitted turbulence intensity profiles closely matched the various standards. However, they observed a faster decline in the turbulence intensity above 40 m in the observation profiles. Luo et al. [14] utilized a meteorological observation gradient tower that stood at a height of 365 m and examined the wind characteristics during the landing of the powerful Typhoon Hato. The researchers discovered that as the average wind velocity exceeded 10 m/s, the measured crest factor was notably lower than the predictions made by Ishizaki [15] and Choi [16]. The reason for this disparity could be the non-gaussian characteristics of wind turbulence. Xia et al. [17] used actual measured data from ultrasonic anemometers at 10, 80, and 100 m above the ground from a wind measurement tower in Fujian to analyze the wind profile of Typhoon Maria and found that index 0.2208 calculated by the power rate was greater than the Chinese standard value. In addition, numerous researchers have also examined wind characteristics, including the turbulence integral scale and wind speed power spectrum, utilizing data obtained from wind towers [18,19].

Wind load as a controlling factor for transmission towers is crucial for enhancing structural resistance against wind. Despite the fact that numerous researchers have extensively studied the field measurement of wind characteristics near ground, variations exist in the wind profiles, turbulence profiles, and peak factors derived from observed typhoons across different terrains and theoretical models. Meanwhile, due to the suddenness and uncertainty of typhoons, collecting typhoon data under field conditions is difficult, leading to a lack of research on the characteristics of near-ground wind fields in coastal areas in China.

This study chose the 550 kV 52# pole transmission tower in Ningde City, Fujian Province as the observation base station. A three-dimensional ultrasonic anemometer was employed to gather wind speed data for Typhoon Soulik at heights of 15, 27, 53, 67, and 82 m above the ground, which was measured at regular intervals of 10 min. A detailed study was conducted on Soulik's wind characteristics, including factors such as wind speed profile, turbulence intensity, gust factor, crest factor, and power spectrum. The organization of this paper is as follows: Section 2 introduces the Typhoon Soulik in 2013, along with the measured locations and instruments utilized. Sections 3 and 4 introduce the average wind characteristics and the fluctuating wind features during Typhoon Soulik, respectively. Section 5 summarizes the research findings.

2. Typhoon Soulik and Field Measurement

Typhoon Soulik (international number 1307) originated in the northwest Pacific on 8 July 2013. At 2:00 on 10 July, it was upgraded to a super typhoon and was moving at a speed of 20 km/h. At 16:00 on 13 July, it first made landfall along the coast of Ningde City, Fujian Province, China, carrying the highest wind speed of 33 m/s. Simultaneously, at 16:20 on the 13th, the observation location experienced a minimum distance of merely 87 km, after which it diminished in intensity and transformed into a tropical storm. Figure 1a depicts the center track of super Typhoon Soulik characterized by great intensity, stable route, and extensive impact.

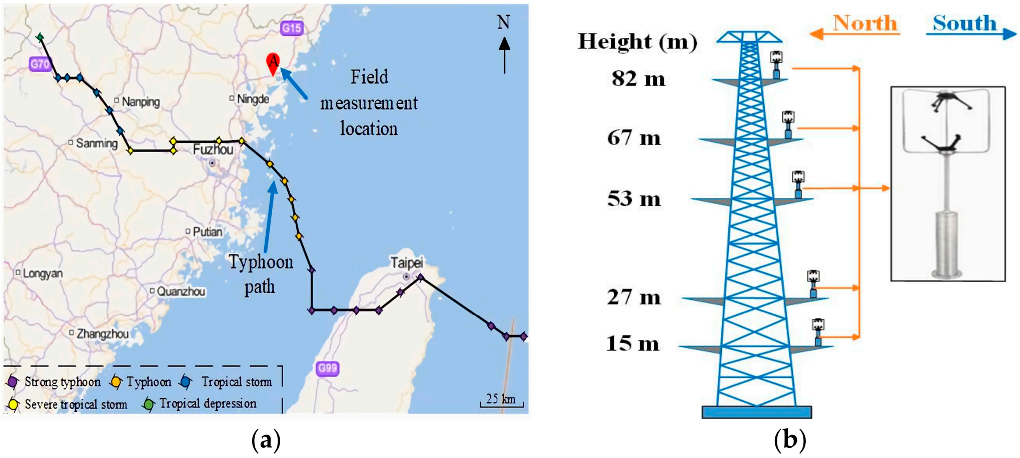

Figure 1. Typhoon Soulik: (**a**) Typhoon center track, and (**b**) Observation tower.

The observation of this typhoon was conducted in collaboration between the State Grid and the China Electric Power Research Institute. The measurement tower was situated in Ningde City, Fujian Province, at coordinates 26°25′ N, 119°46′ E. The measurement site is surrounded by hills in the north and south directions, with open terrain on the east and west sides, characteristic of a typical valley topography. Wind field observations were conducted using a 3D ultrasonic anemometer at heights of 15, 27, 53, 67, and 82 m above ground level on the 550 kV 52# pole transmission tower, as depicted in Figure 1b. The R.M. Young 81000 ultrasonic anemometer was used with a measurement frequency of 10 Hz. The wind velocity can be measured within a range of 0 to 50 m/s, with an observation accuracy of ±0.2 m/s, and the wind direction may be measured within a range of 0° to 359.9°, with an observation accuracy of ±0.3°. The analysis period for the measured wind speed sequence was from 0:00 on 13 July 2013 to 21:00 on 13 July 2013, and the sampling data were recorded with 10 min as the average time interval.

3. Quantitative Analysis of Mean Wind Properties

3.1. Mean Velocity and Orientation of Wind

The three-dimensional ultrasonic wind speed measures wind velocity components in each of the three directions, denoted as v_x, v_y, and v_z. The average wind velocity U and wind direction angle ϕ are computed using the vector decomposition method, leading to the following equations:

$$U = \sqrt{\overline{v_x}^2 + \overline{v_y}^2 + \overline{v_z}^2} \tag{1}$$

$$cos\phi = \frac{\overline{v_x}}{U} \tag{2}$$

$$sin\phi = \frac{\overline{v_y}}{U} \tag{3}$$

where $\overline{v_x}$, $\overline{v_y}$, and $\overline{v_z}$ represent the mean wind velocities of v_x, v_y, and v_z over a duration of 10 min, respectively. The fluctuating wind speed can be calculated using the following formulas:

$$u' = v_x cos\phi + v_y sin\phi - U \tag{4}$$

$$v' = -v_x cos\phi + v_y sin\phi \tag{5}$$

$$w' = v_z - \overline{v_z} \tag{6}$$

where u', v', and w' stand for the fluctuating wind speeds in the longitudinal, transverse, and vertical directions, respectively.

Figure 2 depicts the temporal variations of the 10 min average wind velocity and wind direction at various heights from 0:00 to 21:00 on 13 July. Throughout this time period, the average wind velocity rose in correlation with the height of observation, peaking at its highest point around 13:10 on the 13th. The average wind speeds at heights of 15, 27, 53, 67, and 82 m were recorded as 15.24 m/s, 16.67 m/s, 17.22 m/s, 17.72 m/s, and 18.24 m/s, respectively, with corresponding wind direction angles of 73.58°, 83.23°, 80.9°, 74.21°, and 76.40°. Furthermore, the wind direction angle showed little variation with height and stabilized around 7:00 a.m. on 13 July 2013.

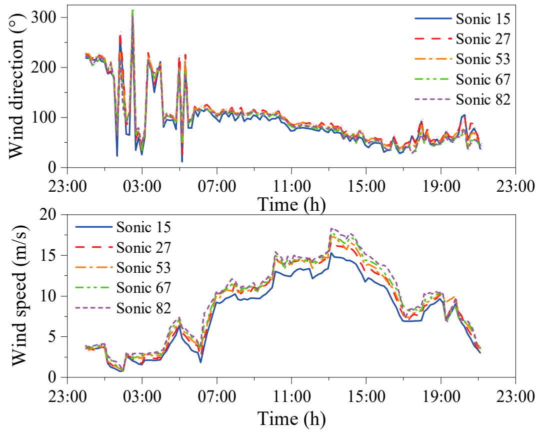

Figure 2. Changes in average wind velocity and direction over time.

3.2. Profiles of Wind Velocity

The wind speed profile represents the vertical arrangement of transverse wind speed and is a crucial factor in calculating wind loads on buildings. Multiple ideas and models have been developed to elucidate the variations in average wind speed with height inside the atmospheric boundary layer. These include the power law [20], the logarithmic law [20], and the Deaves–Harries model [21].

(1) Power law

Through extensive empirical research, Davenport [20] conducted an analysis of wind profiles across various terrains. The findings indicate that the exponential function provides a more accurate representation of the variations in average wind height. The power law expression is

$$\frac{U(z)}{U\left(z_{ref}\right)} = \left(\frac{z}{z_{ref}}\right)^{a} \tag{7}$$

where z_{ref} represents the standard height, $U\left(z_{ref}\right)$ represents the average wind velocity at the standard height, and a represents the power law constant.

(2) Logarithmic law

In a state of neutral atmospheric circumstances, there exists a region where the inner and outer boundary layers overlap. Within this region, the wind velocity adheres to both the boundary layer law and the velocity deficit law. The logarithmic law expression is

$$U(z) = \frac{u^*}{\kappa} In\left(\frac{z}{z_0}\right) \tag{8}$$

where z_0 is the roughness length. This study employs the 0.02 m measurement based on the landform characteristics and the Class C site conditions under the American specification [22]; κ is the von Karman constant, usually 0.4; u^* represents friction speed. Its commonly used mathematical formula is as follows [23].

$$u^* = \left[\left(\overline{u'w'}\right)^2 + \left(\overline{v'w'}\right)^2\right]^{1/4} \tag{9}$$

(3) Deaves–Harries model

The Deaves–Harries model is optimized on the basis of the logarithmic law and can be well applied to the whole boundary layer. The expression is

$$\frac{U(z)}{u^*} = \left(\frac{1}{\kappa}\right)\left\{In\left(\frac{z}{z_0}\right) + 5.75\left(\frac{z}{z_g}\right) - 1.88\left(\frac{z}{z_g}\right)^2 - 1.33\left(\frac{z}{z_g}\right)^3 + 0.25\left(\frac{z}{z_g}\right)^4\right\} \quad (10)$$

where z_g denotes the boundary layer height, which is computed as follows:

$$z_g = \frac{u^*}{B'f} \quad (11)$$

where B' is the empirical parameter, generally six, and f is the Coriolis parameter, which is taken as $7.554 \times 10^{-5} s^{-1}$ in this study.

Figure 3a displays variation trends in average wind speed with height in five distinct groups. From the figure, the measured wind speed profile presents two different changing trends. As the wind speed is below 12 m/s, the average wind speed exhibits a very gradual variation with height. However, as it exceeds 12 m/s, the variation becomes more pronounced. Figure 3b displays the comparative graph of the measured wind profile and each standard. The findings indicate that as the average wind speed exceeds 12 m/s, the power law and the logarithmic law demonstrate a closer fit to the observed variation pattern of Typhoon Soulik's average wind speed with height, but the Deaves–Harris model exhibits some disparities.

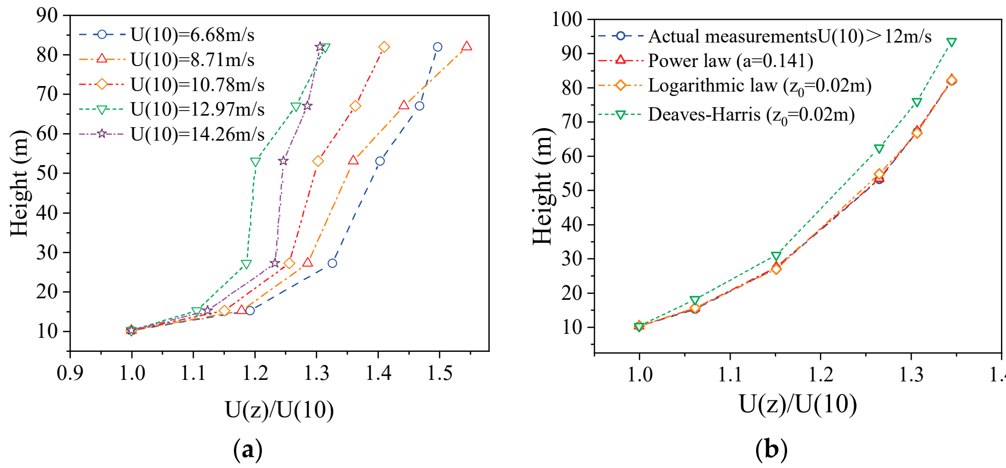

Figure 3. Comparison between measured results and theoretical results of wind profiles at different wind speeds: (**a**) Different wind profile, and (**b**) Measured and theoretical results.

To establish a quantitative assessment of the degree of concurrence between the theoretical model and the measured wind profile, the power law, the logarithmic law, and the Deaves–Harries model are evaluated with the measured wind profile. The wind speed correlation coefficient and standard deviation of the theoretical model are represented by a Taylor diagram, as shown in Figure 4. From the figure, the Deaves–Harris model shows the lowest correlation coefficient with measured wind profiles at 0.49 and the highest normalized standard deviation at 0.44. The power law and the logarithmic law both exhibit correlation coefficients of around 0.7 with measured wind profiles, while their normalized standard deviations are 0.11 and 0.09, respectively. This indicates a higher level of agreement with the measured wind profiles. Meanwhile, there are errors of 1.01 m/s, 0.94 m/s, and 1.57 m/s in the root mean square of the estimated power law, the logarithmic law, and the Deaves–Harries model, respectively. The findings indicate that the power law and the logarithmic law provide a more precise description of the observed wind profiles, consistent with the findings of Lin et al. [12] on wind profiles at the time of typhoon landfall. Conversely, the Deaves–Harries model demonstrates a poorer fit with the actual wind profiles.

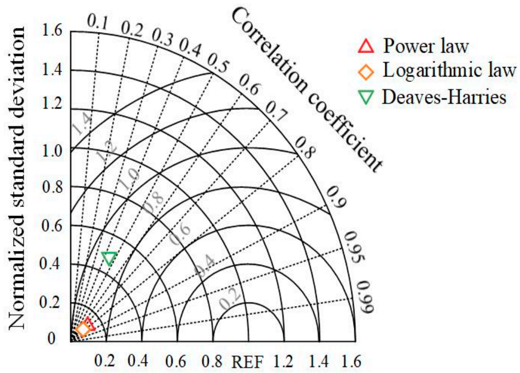

Figure 4. Correlation coefficients and normalized standard deviation distribution Taylor plots of each standard and measured wind profiles.

4. Quantitative Analysis of Fluctuating Wind Properties

4.1. Variations in the Intensity of Turbulence

The turbulence intensity represents an indicator that quantifies the characteristic of turbulence and serves as a crucial metric for assessing wind loads in structural engineering. It is defined as the ratio of the standard deviation of component velocities to the mean wind velocity during a certain period of time. The expression is

$$I_i = \frac{\sigma_i}{U}(i = u, v, w) \tag{12}$$

where $I_i(i = u, v, w)$ represents the turbulence intensity for every orientation and σ_i denotes the RMS of the turbulence components.

Figure 5 shows the varying trends in turbulence intensity in each direction and the average wind speed through a 10 min period at heights of 15, 27, 53, 67, and 82 m. From the figure, the turbulence intensity of u, v, and w orientations exhibits a strong association with variations in average wind velocity. Furthermore, as the average wind speed drops below 12 m/s, the turbulence intensity diminishes in u, v, and w orientations. Conversely, as it exceeds 12 m/s, the turbulence intensity remains relatively constant.

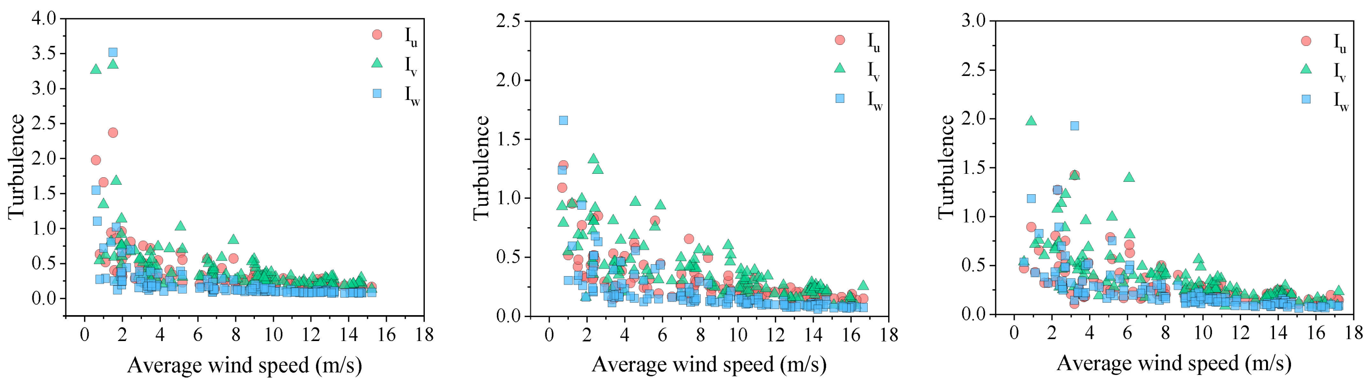

(**a**) (**b**) (**c**)

Figure 5. *Cont*.

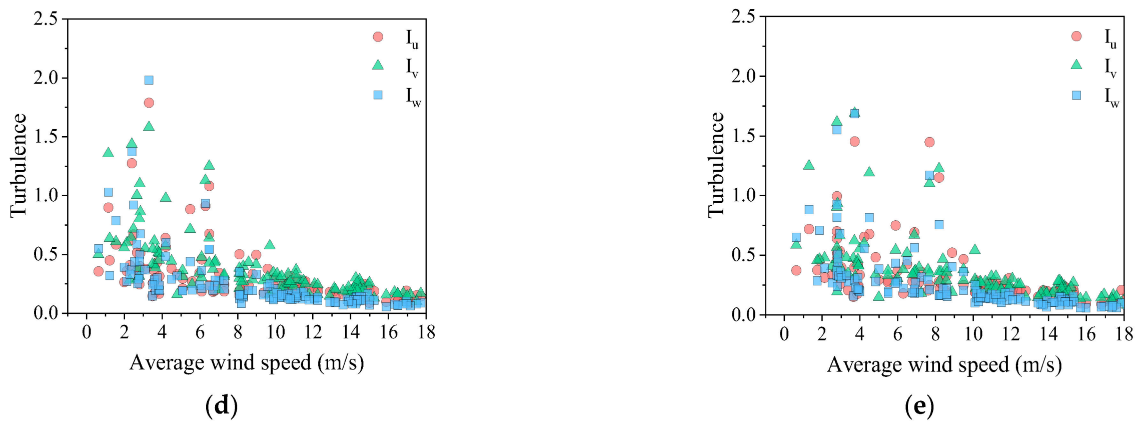

Figure 5. Turbulence intensity changes with average wind speed: (**a**) 15 m, (**b**) 27 m, (**c**) 53 m, (**d**) 67 m, and (**e**) 82 m.

Table 1 displays the recorded ratio of turbulence intensity in each direction at different elevations, together with the outcomes of other research works. The study revealed that the turbulence intensity ratios of Typhoon Soulik in the transverse and longitudinal directions were both over one, which is inconsistent with the findings of Cao et al. [24], Wang et al. [18], and Lin et al. [12]. This may be attributed to the study being situated in a valley terrain and in the peripheral region of the typhoon. Meanwhile, the ratio of vertical to longitudinal turbulence intensity falls within the range of 0.66–0.86, which aligns with the findings of Lin et al. [12].

Table 1. Turbulence intensity ratio.

Researcher	Typhoon	Height (m)	I_u:I_v:I_w	Location
Cao et al. [24]	Maemi	10	1:0.83:0.56	Japan
Wang et al. [18]	Meari	40	1:0.9:0.50	Shanghai, China
Lin et al. [12]	Haitang	32	1:0.83:0.56	Fujian, China
		15	1:1.28:0.66	
Present Results	Soulik	53	1:1.31:0.84	Fujian, China
		82	1:1.17:0.86	

Based on the actual measurements of turbulence at various heights, box plots are drawn; they show the variation in longitudinal, transverse, and vertical turbulence intensity with height, as shown in Figure 6. From the figure, it can be seen that there is a gradual decrease in turbulence intensity as height increases. However, this decline is less significant compared to the variation in turbulence intensity with average wind velocity. Additionally, the comparison is as follows: transverse turbulence intensity > longitudinal turbulence intensity > vertical turbulence intensity. This could be due to the influence of valley topography, causing airflow to become non-uniform, thereby intensifying transverse turbulence. Frequency spectrum analysis of longitudinal and transverse wind components is conducted using Fourier transform, as shown in Figure 7. From the figure, it can be observed that the transverse wind spectrum at heights of 15, 53, and 82 m is higher than the longitudinal wind spectrum, indicating that the transmission tower is more susceptible to transverse wind effects, which may lead to an increase in transverse vibration of the structure. Therefore, in future structural designs, it is advisable to strengthen protection against transverse wind loads.

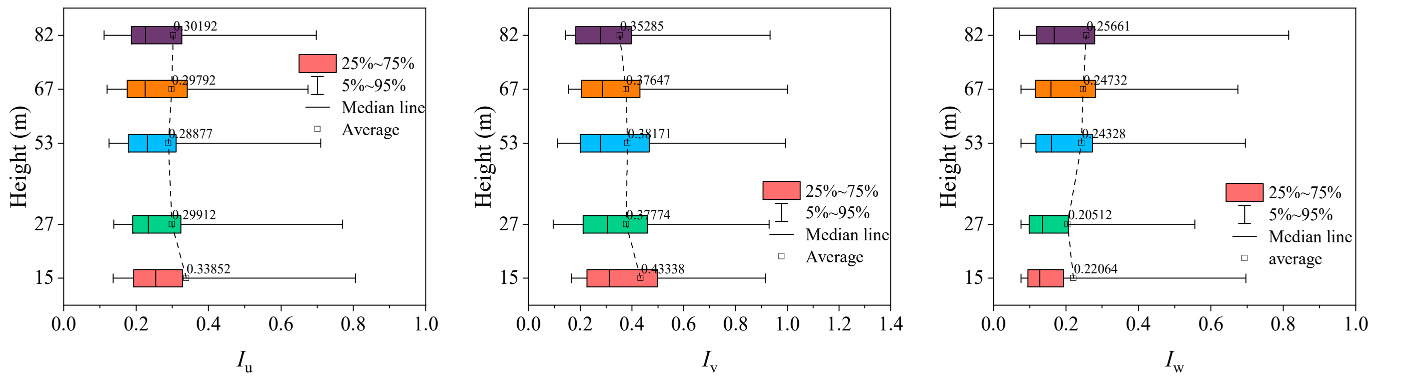

(**a**) (**b**) (**c**)

Figure 6. Distribution of turbulence with height: (**a**) Longitudinal, (**b**) Transverse, and (**c**) Vertical.

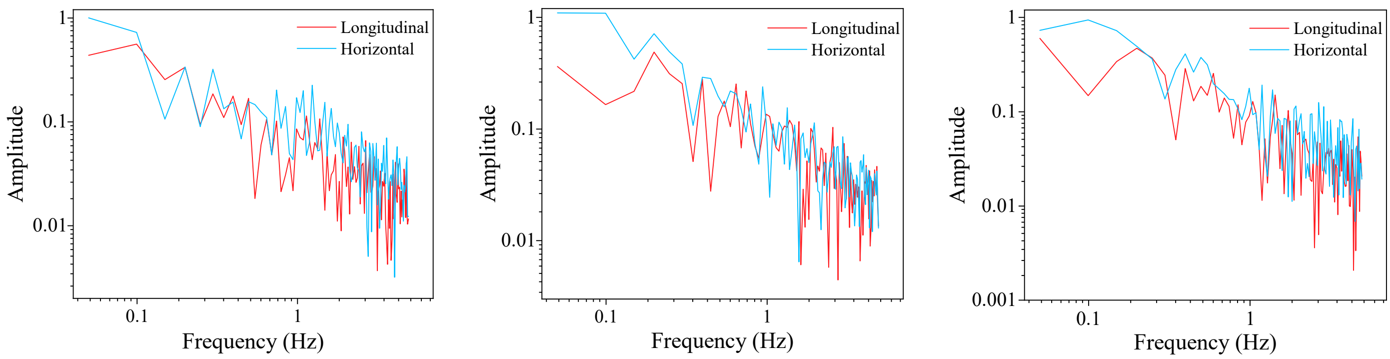

(**a**) (**b**) (**c**)

Figure 7. Wind speed spectrum analysis at different heights: (**a**) 15 m, (**b**) 53 m, and (**c**) 82 m.

To date, numerous national standards have derived the empirical equation for longitudinal turbulence strength as a function of height. Table 2 displays the empirical formulas that indicate the change in turbulence strength with height as stated in the ASCE-7 [22], AIJ2004 [25], and Eurecode standards [26], respectively. Based on the landform type in this study, c is 0.2 in the ASCE-7 standard. In the AIJ2004 standard, a is 0.15, z_g is 350 m, and z_b is 5 m. z_0 in the Eurecode standard is 0.05 m.

Table 2. The empirical formula of turbulence intensity with height in the specification.

Country	Standard	Empirical Expression
American [22]	ASCE-7	$I_u = c(10/z)^{1/6}$
Japanese [25]	AIJ2004	$I_u = 0.1\left(z_b/z_g\right)^{-a-0.05}$
European [26]	Eurecode	$I_u = \frac{1}{In(z/z_0)}$

Combining the empirical formulas of each standard turbulence intensity variation with height, the relationship curve of the measured longitudinal turbulence degree with height is drawn, as shown in Figure 8. As shown, there is a decrease in longitudinal turbulence as height increases. The fitting curve shows the greatest deviation from the European standard while closely resembling the ASCE-7 and AIJ2004 standards. However, there are variations between the measured levels of longitudinal turbulence and the normative empirical values at different heights. Below a height of 53 m, the standard values in ASCE-7 and AIJ2004 exceed the measured values; however, above 53 m, the standard values approach the measured values. The turbulence profile of Typhoon Soulik cannot be characterized by three national standard empirical expressions. Therefore, to derive an empirical expression for the correlation between turbulence intensity and height in typhoons, an approach of exponential fitting is used to assess the longitudinal degree of turbulence. The outcomes for fitting are displayed in Table 3.

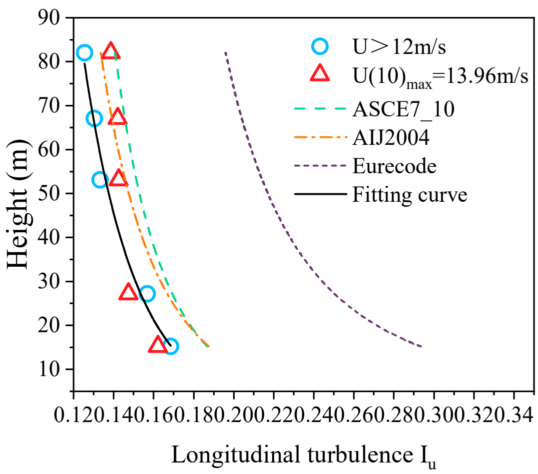

Figure 8. Longitudinal turbulence varies with height.

Table 3. Formula for fitting turbulence intensity.

Typhoon	Direction of Turbulence	Formula
Soulik	I_u	$I_u = 0.01(\frac{0.7}{z})^{4.97}$
	I_v	$I_v = 0.06(\frac{0.7}{z})^{4.42}$
	I_w	$I_w = 0.07(\frac{0.7}{z})^{2.73}$

At the same time, there are few studies on the changes in transverse and vertical turbulence degrees with height, and there is a lack of corresponding empirical expressions. Therefore, this study performs a similar exponential fitting on the measured results of transverse and vertical turbulence. The fitting outcomes are shown in Figure 9. The levels of transverse and vertical turbulence through fitting are presented in Table 3.

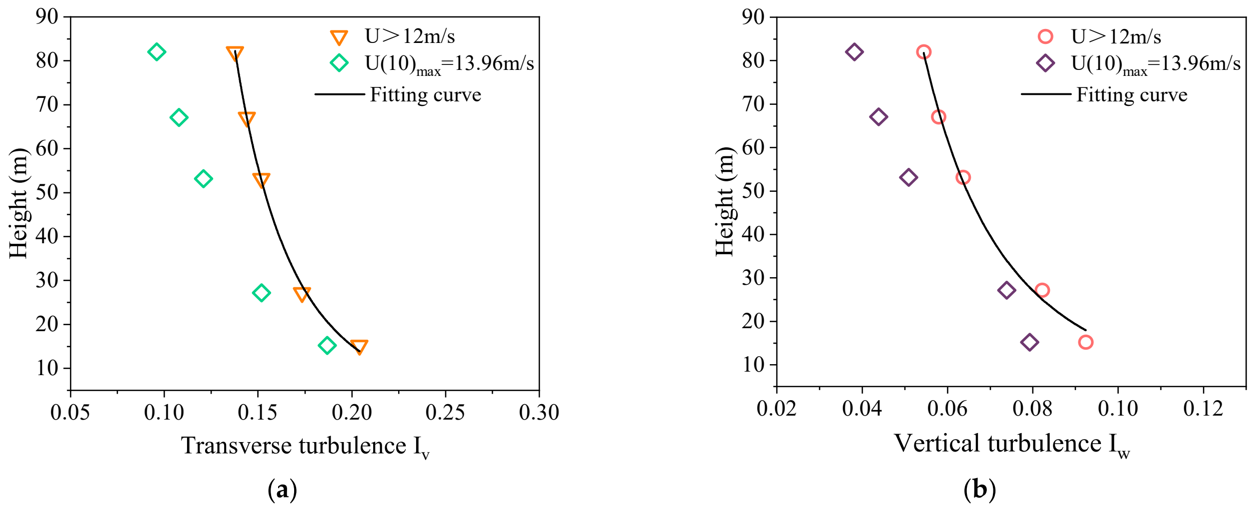

Figure 9. Turbulence variation with altitude and the fitting curve: (**a**) Transverse and (**b**) Vertical.

4.2. Variations in the Gust Factor

The gust factor is strongly associated with the intensity of turbulence and serves as a crucial measure of gust strength. It is defined as the ratio of the average peak wind velocity to the average wind velocity over a specified time period t_g. Its expression is as follows:

$$G_u = 1 + \frac{\overline{maxu(t_g)}}{U} \tag{13}$$

$$G_v = 1 + \frac{\overline{maxv(t_g)}}{U} \tag{14}$$

$$G_w = 1 + \frac{\overline{maxw(t_g)}}{U} \tag{15}$$

where $\overline{maxu(t_g)}$, $\overline{maxv(t_g)}$, and $\overline{maxw(t_g)}$, respectively, represent the average highest wind speed of longitudinal, transverse, and vertical fluctuating winds.

Figure 10 depicts the variations in longitudinal, transverse, and vertical gust components in relation to average wind velocity at different heights. From the figure, it can be seen that there is a progressive drop in each direction gust factor as the average wind velocity increases, aligning with the research outcomes of Fang et al. [13]. As the average wind velocity is below 12 m/s, the gust factor diminishes more rapidly. Conversely, as the average wind velocity exceeds 12 m/s, the relationship with the average wind velocity tends to remain constant.

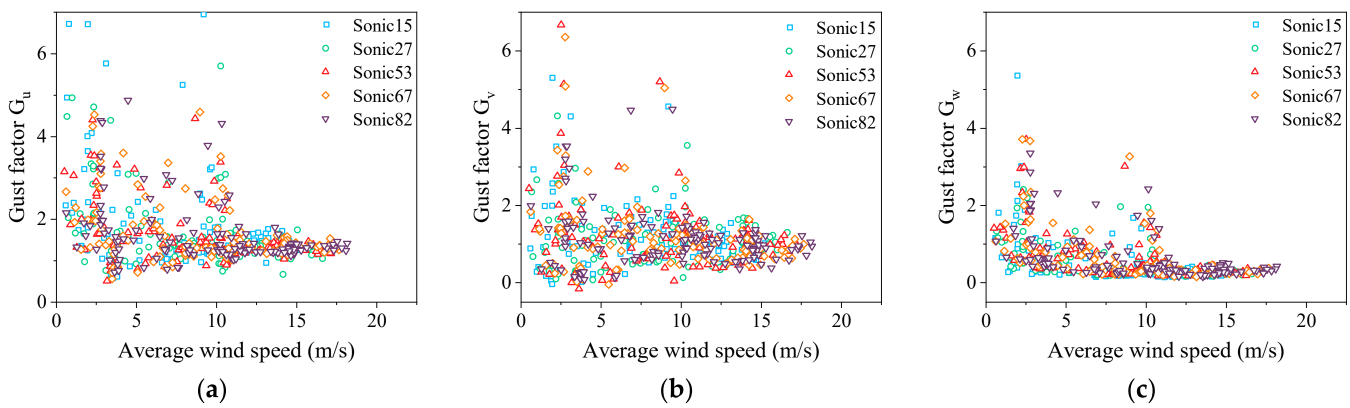

Figure 10. Relationship between gust factor and average wind velocity: (**a**) Longitudinal, (**b**) Transverse, and (**c**) Vertical.

Figure 11 depicts the observed variations in the gust factor of height and fitting curves. From the figure, it can be observed that the gust components in u, v, and w orientations diminish as the height rises. Since the expression of the gust factor profile is not yet clear, this study fits the various gust factors in the form of $G_i = a\left(\frac{z}{10}\right)^{\beta}$. The study demonstrates that the changes observed in the gust factors for u, v, and w orientations with height align with the fitting results. This suggests that the equation can accurately describe the changes in Typhoon Soulik's gust factor with height. The results of the fitting expression are presented in Table 4.

Table 4. Formula for fitting gust factor.

Researcher	Direction	Expression
Present Results	Longitudinal	$G_u = 2.17\left(\frac{z}{10}\right)^{-6.67}$
	Transverse	$G_v = 3.76\left(\frac{z}{10}\right)^{-5.03}$
	Vertical	$G_w = 6.4\left(\frac{z}{10}\right)^{-6.52}$

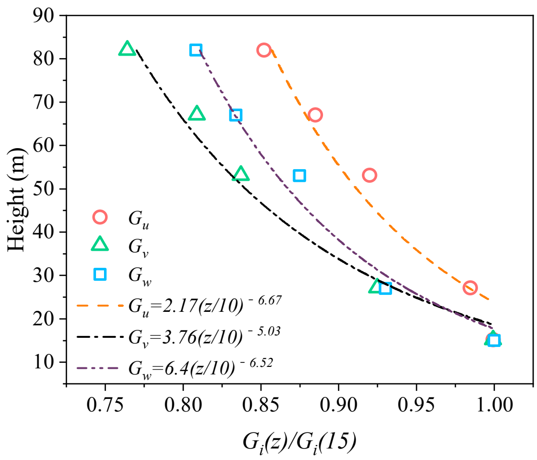

Figure 11. Relationship between gust factor, height, and fitting curve.

4.3. Correlation between Turbulence Intensity and Gust Factor

The following describes the correlation with gust factor and turbulence degree:

$$G_u = 1 + aI_u^b In(T/t_g) \tag{16}$$

where T denotes the mean duration of wind and t_g denotes the sustained time interval. According to Ishizaki [15], there is a linear correlation between the two variables, and it is recommended that a be 0.5 and b be 1.0. Choi [16] enhanced Equation (16) by utilizing observational data and proposed that the value of a should be 0.62 while the value of b should be 1.27. Cao et al. [24] examined the properties of high winds near the ground during Typhoon Maemi and employed Equation (16) to establish an association between two variables. The analysis yielded fitting parameters of $a = 0.5$ and $b = 1.15$.

Figure 12 depicts the association between two variables at heights of 15, 53, and 82 m along with the corresponding empirical curves. As shown, the gust factor increases with the intensity of turbulence and exhibits a linear correlation. When the turbulence intensity is below 0.5, the fitting curve and the empirical curve of Choi and Ishizaki are essentially similar. When the turbulence intensity exceeds 0.5, the fitting curve aligns more closely with Choi's empirical formula at heights of 15, 53, and 82 m. This suggests that the findings of this study are in greater agreement with Choi's empirical formula. Furthermore, the collected data are analyzed using Equation (16), and coefficients a and b are obtained for heights of 15, 53, and 82 m, as indicated in Table 5.

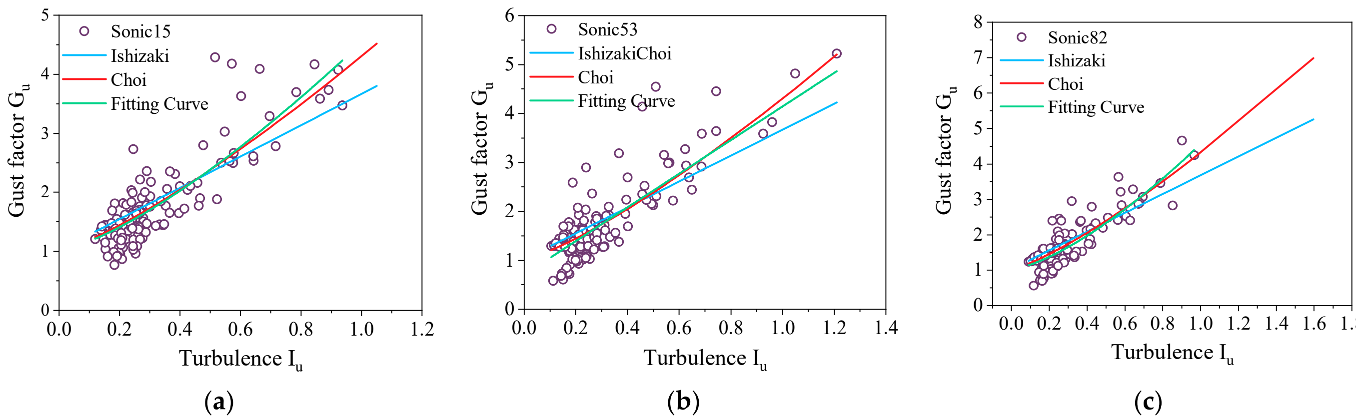

Figure 12. Gust factor variation with the intensity of turbulence: (**a**) 15 m, (**b**) 53 m, and (**c**) 82 m.

Table 5. Fitting parameters *a* and *b*.

Typhoon	Height (m)	*a*	*b*
Soulik	15	0.862	1.291
	53	0.759	1.203
	82	0.718	1.361

4.4. Variations in the Crest Factor

The instantaneous intensity of fluctuating wind can be described by the crest factor, which has the following expression:

$$g_u = \left(\overline{U_{t_g}} - U\right)/\sigma_i \tag{17}$$

where σ_i represents the longitudinally fluctuating wind velocity standard deviation and $\overline{U_{t_g}}$ represents the average highest velocity of the wind for that interval of time t_g.

Figure 13 shows the correlation among gust factor, average wind speed, and height. From Figure 13a, at heights of 15, 27, 53, 67, and 82 m, the variations in the peak factor with respect to the average velocity of the wind are comparatively dispersed. As the average wind velocity is below 6 m/s, the peak factor diminishes as the average wind speed rises and thereafter stabilizes at a value of around 1.5. From Figure 13b, it can be seen that there is a progressive decline in the peak factor as the observation height increases. The peak factor has an average value of 1.87 at 15 m and an average value of 1.67 at 82 m.

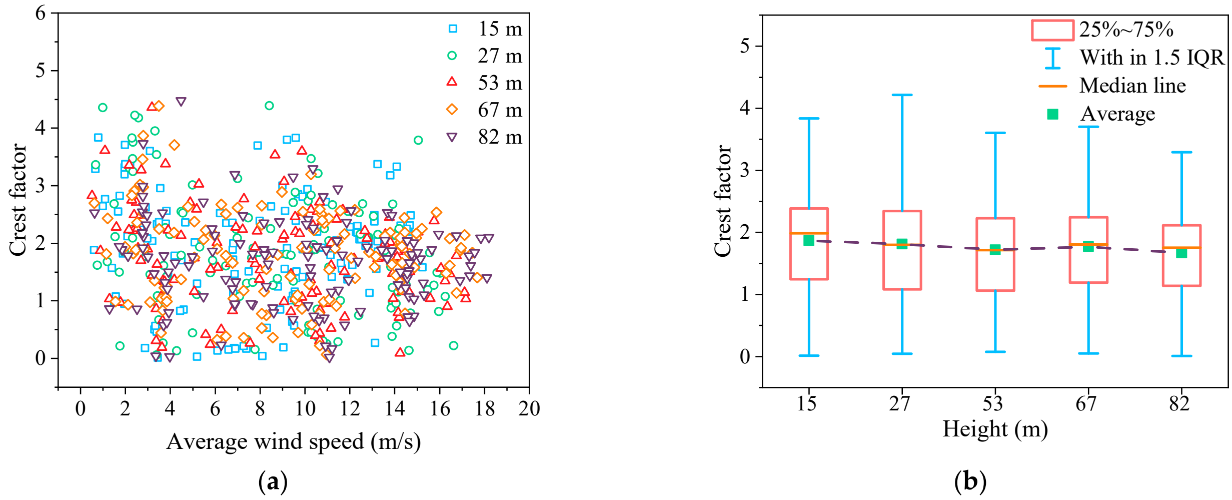

Figure 13. The change in crest factor: (**a**) Average wind speed and (**b**) Height.

To study whether fluctuating wind speeds under the influence of a typhoon follow a Gaussian distribution, Figure 14 depicts the probability density distributions of longitudinal fluctuating wind speeds at heights of 15, 53, and 82 m. Gaussian function distribution curves are obtained using moment estimation. From the figure, it can be observed that the probability density distributions of longitudinal fluctuating wind speeds align well with Gaussian function curves, indicating that the probability density distribution of fluctuating wind speeds during Typhoon Soulik conforms to a Gaussian distribution. Meanwhile, the probability density distributions of transverse and vertical fluctuating wind speeds are consistent with Gaussian distributions which are not shown in this paper.

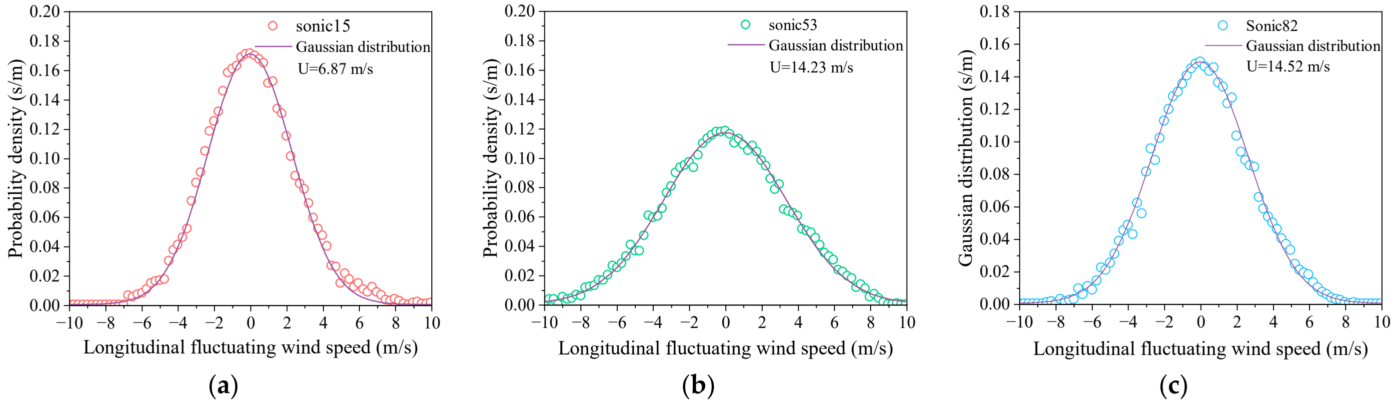

Figure 14. Probability density distribution of longitudinal fluctuating wind speed at each height: (**a**) 15 m, (**b**) 53 m, and (**c**) 82 m.

4.5. Variations in the Turbulence Integral Scale

The turbulence integral scale represents the mean dimensions of each turbulent eddy and is a significant parameter that reveals the attributes of the wind field. This study employs the autocorrelation function method to integrate it and uses the Taylor hypothesis to turn the time scale into a length scale. The expression is

$$L_i = \frac{U}{\sigma_i^2}\int_0^{\infty} R_i(\tau)d\tau \tag{18}$$

where L_i denotes the integral scale components of turbulence in the u, v, and w orientations, and $R_i(\tau)$ denotes the fluctuating wind speed autocorrelation function.

Figure 15 displays variations in the scales of turbulence in all directions at heights of 15, 53, and 82 m. It can be observed from the graphic that the longitudinal, transverse, and vertical turbulence integral scales exhibit an upward trend with average wind velocity. Additionally, the distribution becomes progressively more discontinuous. The longitudinal turbulence integral scale exhibits more pronounced fluctuations compared to the transverse and vertical components.

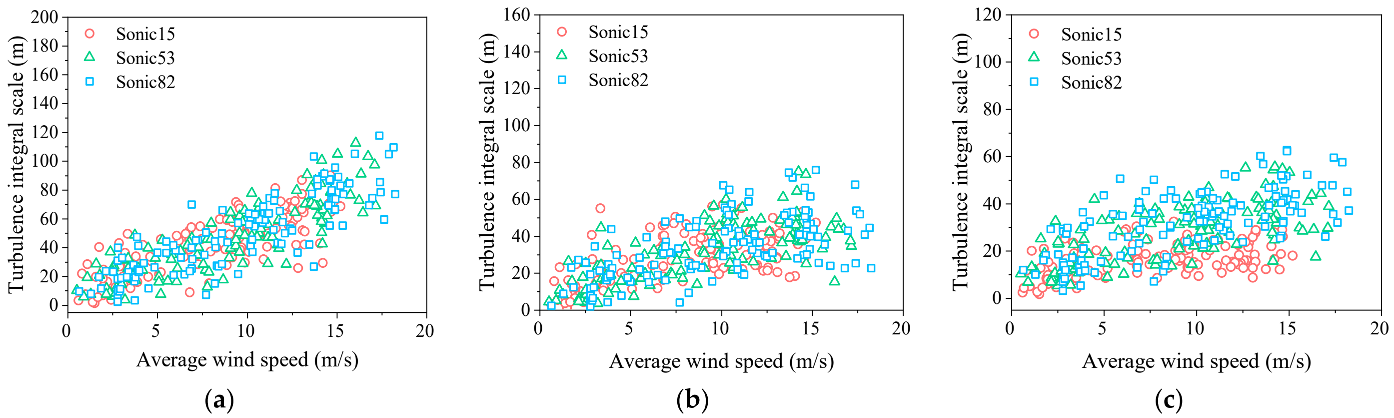

Figure 15. Changes in the integral scale of turbulence with the average wind speed: (**a**) Longitudinal, (**b**) Transverse, and (**c**) Vertical.

Figure 16 depicts the probability density distribution of the integral scale of turbulence. It can be clearly found that the probability density distribution range of the longitudinal and transverse turbulence integral scales is much larger than that of the vertical direction. At the same time, the probability density distribution at different observation heights is basically the same, and the distribution range becomes wider and wider as the observation altitude increases. Simultaneously, the integral scale of turbulence increases proportionally with altitude, aligning with the findings of Wang et al. [18].

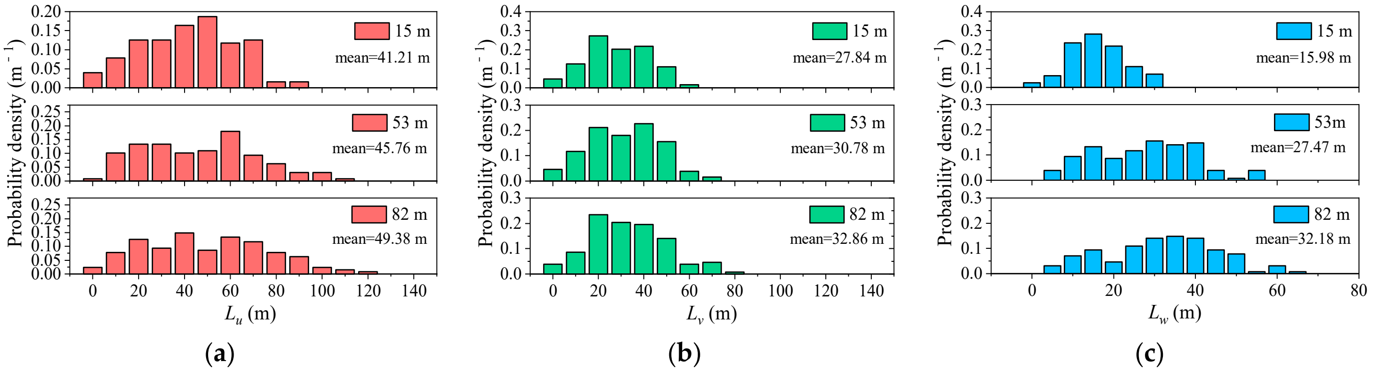

Figure 16. Probability density distribution diagram of integral scale of turbulence in various orientations: (**a**) Longitudinal, (**b**) Transverse, and (**c**) Vertical.

This study aims to validate the accuracy of the scale by calculating the ratio of the measured longitudinal, transverse, and vertical turbulence integral scales. The obtained ratios are then compared with the findings of other researchers, as presented in Table 6. The integral scales of turbulence differ between distinct typhoons and strong winds, as seen in the table. The turbulence intensity ratios measured in this study are higher than those that Kato et al. [27], Hui et al. [28], and Song et al. [29] researched. The ratio closely approximates that of Wang et al. [30], possibly attributed to the roughness of the underlying terrain, the type of the wind field, and the observation height.

Table 6. Ratio of integral length scales in each direction of turbulence.

Researcher	Wind Type	Observed Altitude (m)	L_u:L_v:L_w
Kato et al. [27]	Typhoon	55.7	1:0.33:0.17
		86.0	1:0.50:0.17
Hui et al. [28]	Strong breeze	50	1:0.46:0.19
Song et al. [29]	Typhoon	60	1:0.66:0.16
Wang et al. [30]	Typhoon	10	1:0.69:0.08
		20	1:0.61:0.09
		40	1:0.65:0.13
Presents Results	Typhoon	15	1:0.68:0.11
		53	1:0.67:0.27
		83	1:0.67:0.30

4.6. Turbulence Integral Scale

4.6.1. Auto Spectrum

The turbulence power spectrum provides a more precise description of the characteristics of fluctuating wind by representing the energy distribution on various scales. Its expression is as follows:

$$\frac{s_u(f)}{u^2} = \frac{A}{\left(1 + Bf^{\beta}\right)^{\gamma}} \tag{19}$$

where f represents frequency and A, B, β, and γ represent four parameters.

Numerous studies [14,25] have shown that the Von Karman spectrum provides an excellent description of the energy distribution of turbulence in typhoons, and its expression is as follows [31]:

$$s_u(n) = \frac{2\overline{u'^2} L_u^x}{\overline{U}\left[1 + \left(2cnL_u^x/\overline{U}\right)\right]^{5/6}} \tag{20}$$

where $\overline{U}$ denotes the average wind velocity and L_u^x denotes the average wind velocity on the longitudinal turbulence integration scale.

To check whether the fluctuating wind speed of this typhoon adheres to the Von Karman empirical spectrum, Figure 17 depicts the longitudinally fluctuating wind velocity, along with comparison curves of the empirical spectrum, for heights of 15, 53, and 82 m. Based on the figure, the longitudinal fluctuating velocity of the wind spectra at heights of 15, 53, and 82 m coincides with the empirical spectra. Within the upper frequency range, the value is notably greater than the empirical spectrum value, while within the lower frequency range the value is notably smaller than the empirical spectrum value. This observation aligns with the outcomes of Wang et al. [30] about Typhoon Meari. Furthermore, the features of transverse and vertically fluctuating wind velocity power spectra are similar, which will not be reiterated. In general, the Von Karman empirical spectrum is applicable for describing the fluctuating wind velocity of Typhoon Soulik.

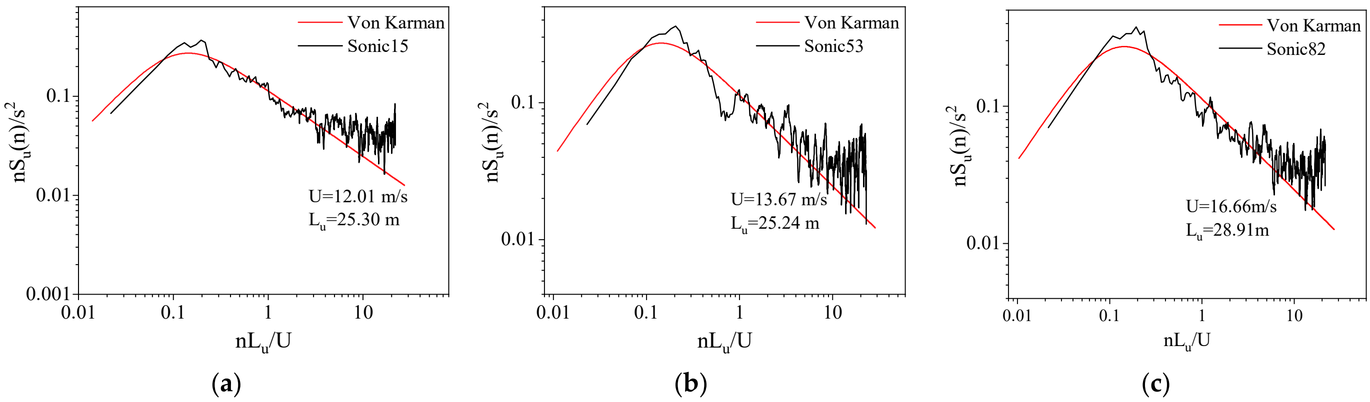

Figure 17. Longitudinal power spectra: (**a**) 15 m, (**b**) 53 m, and (**c**) 82 m.

4.6.2. Cross-Spectrum

There is a limited number of studies on the cross-spectrum of fluctuating wind velocity in the field of studying wind characteristic parameters. Kaimal et al. [32] used normal wind experimental data to derive the expressions for the fluctuating wind speed cross-spectrum:

$$\frac{-nC_{uw}(n)}{u^{*2}} = \frac{14f}{(1+9.6f)^{2.4}} \tag{21}$$

where C_{uw} represents the cross-spectrum, u^{*2} represents friction velocity, and f is frequency.

After trial calculation, it was observed that there exists a distinct discrepancy between the recorded cross-spectrum of fluctuating wind velocity and the spectrum value derived using Kaimal's empirical spectrum. To enhance the precision of the fluctuating wind velocity cross-spectrum, the Kaimal empirical spectrum was modified. Therefore, this study proposes the following improvement to Equation (21):

$$\frac{-nC_{uw}(n)}{\sigma_u^2} = \frac{af}{(1+bf)^c} \tag{22}$$

where σ_u is about $2.5U_0^*$ and variables a, b, and c are sample fitting parameters.

This study employs 10 min sample data to fit the three parameters, a, b, and c, at different heights and derives the cross-spectrum expressions of longitudinal and transverse fluctuating wind velocity at heights of 15, 53, and 82 m. The outcomes are presented in Table 7.

Table 7. Fitting parameters and mathematical expressions.

Height (m)	*a*	*b*	*c*	Kaimal
15	2.4	65.4	1.29	$\frac{-nC_{uw}(n)}{\sigma_u^2} = \frac{2.4f}{(1+65.4f)^{1.29}}$
53	5.1	45.9	1.62	$\frac{-nC_{uw}(n)}{\sigma_u^2} = \frac{5.1f}{(1+45.9f)^{1.62}}$
82	3.1	44.3	1.61	$\frac{-nC_{uw}(n)}{\sigma_u^2} = \frac{3.1f}{(1+44.3f)^{1.61}}$

Figure 18 shows the cross-spectrum and modified Kaimal spectrum function curves of wind velocity at heights of 15, 53, and 82 m. From the figure, it can be seen that the measured fluctuating wind speed cross-spectrum and the modified Kaimal spectrum agree well in all frequency bands, indicating the modified Kaimal spectrum may accurately represent the fluctuating wind cross-spectrum of Typhoon Soulik.

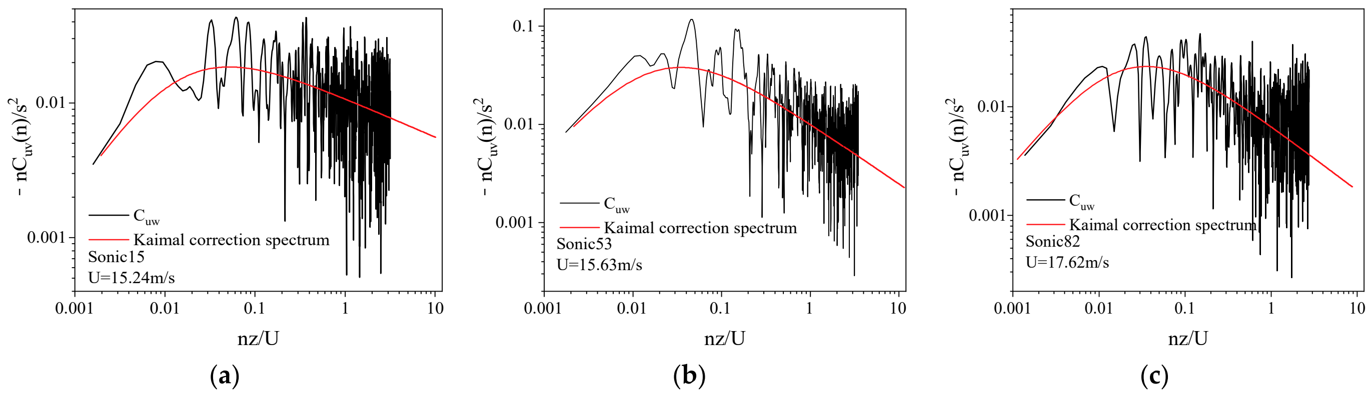

Figure 18. Power spectra at different heights: (**a**) 15 m, (**b**) 53 m, and (**c**) 82 m.

5. Conclusions

Based on 10 min wind field data at heights of 15, 27, 53, 67, and 82 m in China's coastal areas, wind field characteristics such as Typhoon Soulik's wind speed profile, turbulence intensity, gust factor, peak factor, and turbulence integral scale were analyzed. The following significant conclusions were made:

(1) When the mean wind velocity exceeded 12 m/s, Typhoon Soulik's average wind speed variation trend with height aligned with both the power law and the logarithmic law. However, the Deaves–Harris model showed significant differences.

(2) The gust components in u, v, and w orientations fitted in the form of $G_i = a\left(\frac{z}{10}\right)^{\beta}$ approximately coincided with the changes in measured gust factors with height. Furthermore, the measured data were utilized to examine the correlation between gust factor and turbulence intensity, and these findings were then compared to previous study outcomes. The results were found to be consistent with Choi's empirical formula.

(3) The integral scale of turbulence in u, v, and w orientations was positively correlated with both the average wind velocity and height. The integral scales of turbulence in all directions at heights of 15, 53, and 82 m had ratios of 1:0.68:0.11, 1:0.67:0.27, and 1:0.67:0.30, respectively.

(4) A power spectrum analysis was performed on the fluctuating wind velocity near the ground during Typhoon Soulik. The results revealed that the von Karman spectrum effectively depicted the power spectrum of wind velocity. Also, the modified Kaimal cross-spectrum model showed excellent concordance with the observed cross-spectrum in all ranges of frequencies.

Author Contributions: Conceptualization, X.W.; writing—original draft preparation, Z.Y.; supervision, Y.G.; writing—review and editing, Y.L. All authors have read and agreed to the published version of the manuscript.

Funding: This paper was partially supported by the Natural Science Foundation of Chongqing (Grant No.: CSTB2022NSCQ-MSX1655) and the State Key Laboratory of Structural Dynamics of Bridge Engineering and Key Laboratory of Bridge Structure Seismic Technology for Transportation Industry Open Fund (Grant No.: 202205).

Institutional Review Board Statement: Not applicable.

Informed Consent Statement: Not applicable.

Data Availability Statement: All data generated or analyzed during this study are included in this article. All data included in this study are available upon request by contact with the corresponding author.

Conflicts of Interest: The authors declare no conflicts of interest.

References

1. Chen, T.; Fu, J.Y.; Chan, P.W.; He, Y.C.; Liu, A.M.; Zhou, W. Wind characteristics in typhoon boundary layer at coastal areas observed via a Lidar profiler. *J. Wind Eng. Ind. Aerodyn.* **2023**, *232*, 105253. [CrossRef]
2. He, J.Y.; Chan, P.W.; Li, Q.S.; Li, L.; Zhang, L.; Yang, H.L. Observations of wind and turbulence structures of Super Typhoons Hato and Mangkhut over land from a 356 m high meteorological tower. *Atmos. Res.* **2022**, *265*, 105910. [CrossRef]
3. Yi, G.; Pan, J.; Zhao, L.; Song, L.; Fang, G.; Cui, W.; Ge, Y. Profiles of mean wind and turbulence intensity during strong typhoon landfall. *J. Wind Eng. Ind. Aerodyn.* **2022**, *228*, 105106. [CrossRef]
4. Wu, J.; Hu, N.; Dong, Y.; Zhang, Q.; Yang, B. Wind characteristics atop Shanghai Tower during typhoon Jongdari using field monitoring data. *J. Build. Eng.* **2021**, *33*, 101815. [CrossRef]
5. Norén-Cosgriff, K.; Kaynia, A.M. Estimation of natural frequencies and damping using dynamic field data from an offshore wind turbine. *Mar. Struct.* **2021**, *76*, 102915. [CrossRef]
6. Blocken, B. 50 years of computational wind engineering: Past, present and future. *J. Wind Eng. Ind. Aerodyn.* **2014**, *129*, 69–102. [CrossRef]
7. Dai, G.; Xu, Z.; Chen, Y.F.; Flay, R.G.; Rao, H. Analysis of the wind field characteristics induced by the 2019 Typhoon Bailu for the high-speed railway bridge crossing China's southeast bay. *J. Wind Eng. Ind. Aerodyn.* **2021**, *211*, 104557. [CrossRef]
8. Wang, X.; Zhang, G.; Li, Y.; Kong, H.; Liu, L.; Zhang, C. Field Measurements of Wind-Induced Responses of the Shanghai World Financial Center during Super Typhoon Lekima. *Sensors* **2023**, *23*, 6519. [CrossRef] [PubMed]
9. Fang, P.; Jiang, W.; Tang, J.; Lei, X.; Tan, J. Variations in friction velocity with wind speed and height for moderate-to-strong onshore winds based on Measurements from a coastal tower. *J. Appl. Meteorol. Climatol.* **2020**, *59*, 637–650. [CrossRef]
10. Tang, J.; Zhang, J.A.; Aberson, S.D.; Marks, F.D.; Lei, X. Multilevel tower observations of vertical eddy diffusivity and mixing length in the tropical cyclone boundary layer during landfalls. *J. Atmos. Sci.* **2018**, *75*, 3159–3168. [CrossRef]
11. Song, L.; Chen, W.; Wang, B.; Zhi, S.; Liu, A. Characteristics of wind profiles in the landfalling typhoon boundary layer. *J. Wind Eng. Ind. Aerodyn.* **2016**, *149*, 77–88. [CrossRef]
12. Lin, L.; Chen, K.; Xia, D.; Wang, H.; Hu, H.; He, F. Analysis on the wind characteristics under typhoon climate at the southeast coast of China. *J. Wind Eng. Ind. Aerodyn.* **2018**, *182*, 37–48. [CrossRef]
13. Fang, G.; Zhao, L.; Cao, S.; Ge, Y.; Li, K. Gust characteristics of near-ground typhoon winds. *J. Wind Eng. Ind. Aerodyn.* **2019**, *188*, 323–337. [CrossRef]
14. Luo, Y.P.; Fu, J.Y.; Li, Q.S.; Chan, P.W.; He, Y.C. Observation of Typhoon Hato based on the 356-m high meteorological gradient tower at Shenzhen. *J. Wind Eng. Ind. Aerodyn.* **2020**, *207*, 104408. [CrossRef]
15. Ishizaki, H. Wind profiles, turbulence intensities and gust factors for design in typhoon-prone regions. *J. Wind Eng. Ind. Aerodyn.* **1983**, *13*, 55–66. [CrossRef]
16. Choi, E.C.C. Characteristics of typhoons over the South China Sea. *J. Wind Eng. Ind. Aerodyn.* **1978**, *3*, 353–365. [CrossRef]
17. Xia, D.; Dai, L.; Lin, L.; Wang, H.; Hu, H. A field measurement based wind characteristics analysis of a typhoon in near-ground boundary layer. *Atmosphere* **2021**, *12*, 873. [CrossRef]
18. Wang, X.; Huang, P.; Yu, X.F.; Huang, C. Near ground wind characteristics during typhoon Meari: Turbulence intensities, gust factors, and peak factors. *J. Cent. South Univ.* **2017**, *24*, 2421–2430. [CrossRef]
19. Zhao, L.; Cui, W.; Ge, Y. Measurement, modeling and simulation of wind turbulence in typhoon outer region. *J. Wind Eng. Ind. Aerodyn.* **2019**, *195*, 104021. [CrossRef]
20. Davenport, A.G. Rationale for determining design wind velocities. *J. Struct. Div.* **1960**, *86*, 39–68. [CrossRef]
21. Deaves, D.M. Computations of wind flow over changes in surface roughness. *J. Wind Eng. Ind. Aerodyn.* **1981**, *7*, 65–94. [CrossRef]
22. *ASCE/SEI 7-10*; Minimum Design Loads for Buildings and Other Structures. ASCE (American Society of Civil Engineers): Reston, VA, USA, 2010.
23. Payil, M.N. Aerodynamic drag coefficient and roughness length for three seasons over a tropical western Indian station. *Atmos. Res.* **2006**, *80*, 280–293. [CrossRef]
24. Cao, S.; Tamura, Y.; Kikuchi, N.; Saito, M.; Nakayama, I.; Matsuzaki, Y. Wind characteristics of a strong typhoon. *J. Wind Eng. Ind. Aerodyn.* **2009**, *97*, 11–21. [CrossRef]

25. *AIJ-RLB-2004*; Recommendations for Loads on Buildings. AIJ: Tokyo, Japan, 2004.
26. *EN1991-1-4*; "Structural Eurocodes", Eurocode 1: Actions on Structures-General Actions-Part 1–4: Wind Actions. BSI (British Standards Institution): London, UK, 2004.
27. Kato, N.; Ohkuma, T.; Kim, J.R.; Marukawa, H.; Niihori, Y. Full scale measurements of wind velocity in two urban areas using an ultrasonic anemometer. *J. Wind Eng. Ind. Aerodyn.* **1992**, *41*, 67–78. [CrossRef]
28. Hui, M.C.H.; Larsen, A.X.H.F.; Xiang, H.F. Wind turbulence characteristics study at the Stonecutters Bridge site: Part I—Mean wind and turbulence intensities. *J. Wind Eng. Ind. Aerodyn.* **2009**, *97*, 22–36. [CrossRef]
29. Song, L.; Li, Q.S.; Chen, W.; Qin, P.; Huang, H.; He, Y.C. Wind characteristics of a strong typhoon in marine sur-face boundary layer. *Wind Struct.* **2012**, *15*, 1–15. [CrossRef]
30. Wang, X.; Huang, P.; Yu, X.F.; Wang, X.R.; Liu, H.M. Wind characteristics near the ground during typhoon Meari. *J. Zhejiang Univ.-Sci. A* **2017**, *1*, 33–48. [CrossRef]
31. Von Karman, T. Progress in the statistical theory of turbulence. *Proc. Natl. Acad. Sci. USA* **1948**, *34*, 530–539. [CrossRef]
32. Kaimal, J.C.; Wyngaard, J.C.J.; Izumi, Y.; Coté, O.R. Spectral characteristics of surface-layer turbulence. *Q. J. R. Meteorol. Soc.* **1972**, *98*, 563–589. [CrossRef]

Disclaimer/Publisher's Note: The statements, opinions and data contained in all publications are solely those of the individual author(s) and contributor(s) and not of MDPI and/or the editor(s). MDPI and/or the editor(s) disclaim responsibility for any injury to people or property resulting from any ideas, methods, instructions or products referred to in the content.